PROCEDURE TO ASSESS THE ROLE OF RAILWAY PANTOGRAPH COMPONENTS IN GENERATING THE AERODYNAMIC UPLIFT

Marco CARNEVALE, Alan FACCHINETTI, Daniele ROCCHI

Dipartimento di Meccanica, Politecnico di Milano
Via La Masa 1, 20156 Milano, Italy
e-mail marco.carnevale@polimi.it
ph. +39 02 2399 8437 fax +39 02 2399 8492

Please cite this article as:
Procedure to assess the role of railway pantograph components in generating the aerodynamic uplift
By:Carnevale, M. ; Facchinetti, A; Rocchi.
JOURNAL OF WIND ENGINEERING AND INDUSTRIAL AERODYNAMICS
Volume: 160 Pages: 16-29
DOI: 10.1016/j.jweia.2016.11.003
Published: JAN 2017

ABSTRACT

Aerodynamic forces play a big role in determining the value of the mean force acting between the collectors of a railway pantograph and the contact wire, especially for speed higher than 200 km/h. The contact force has to be properly calibrated in order to have a good quality collection of power and low wear of contact strips and contact wire. This paper analyses the pantograph features that mainly affect its aerodynamic behaviour, and their influence on the mean value of the contact force. Wind tunnel experimental tests on a full-scale pantograph and Computational Fluid Dynamic (CFD) simulations in a wind tunnel scenario are carried out for different pantograph configurations, and the contribution of each different part of the pantograph to the mean contact force is investigated. To this end, the feasibility of using the RANS model and steady state simulations is evaluated.

Keywords: railway pantograph; wind tunnel tests; computational fluid dynamics; aerodynamic uplift.

1. INTRODUCTION

In pantograph-catenary operation, the contact force between the carbon strips and the contact wire significantly affects the quality of current collection, as the electrical resistance being inversely proportional to the contact force value. The choice of the mean value of the contact force is a compromise between two different needs: on the one hand, low force values are responsible for arcing, disruption of power collection, and electrical-related wear. On the other hand, high contact force values are responsible for mechanical wear on strips and increased excitation of the overhead

contact line, leading to high dynamic oscillation of the force itself and to important stresses on the interacting systems.

International standards for the assessment of the behaviour of the pantograph-catenary system (e.g. TSI, the EU's Technical Specifications for Interoperability) prescribe limits to the mean value and the standard deviation of the contact force, the latter being strongly dependent on the dynamic interaction of the pantograph-catenary system. Contact force variability should be mitigated as much as possible, in order to avoid low and high contact force peaks. Great efforts have been made in the last decades to optimise the mechanical interaction between pantograph and catenary, by means of modifications to the infrastructure, the optimisation of the pantograph dynamic response, and the fine-tuning of operational parameters. Numerical simulations of the dynamic interaction between pantograph and catenary were instrumental for these goals [1]. Simulations are nowadays based on models and features that are shared and agreed-upon within the scientific and technical international communities [2]. This is so well established today that researchers and international studies have moved their focus to the issue of virtual homologation, with the aim of assessing the dynamic interaction of the pantograph-catenary system by means of numerical simulations and laboratory experiments, such as Hardware-In-the-Loop tests (HIL) [3].

Within this framework, pantograph and overhead line aerodynamics are other important factors responsible for affecting the contact force, both in terms of mean value and dynamic variation [4]. This issue is as relevant as the dynamic interaction between pantograph and catenary, even if only more recently investigated in the literature, concurrently with the spread of high-speed railway networks.

Stationary forces acting on pantograph components are able to change the mean value of the contact force, adding their contribution to the uplift force exerted by the pantograph raising mechanism at the bottom of the articulated frame (normally an air spring). This effect, indicated in the following as *aerodynamic uplift*, is dependent on train speed, pantograph working height [5] and orientation (modern pantographs have an asymmetrical geometry generating different aerodynamic uplifts in

the two orientations in which they can operate). Moreover, the aerodynamic uplift varies when the pantograph enters a tunnel, due to the increase of the velocity of the relative flow. The influence of aerodynamic forces on the mean contact force can be so high, especially in the case of high-speed trains, that it is commonly compensated in order to guarantee operational stability. Attempts to balance the aerodynamic uplift by means of aerodynamic spoilers were proposed, but this was not trivial considering that it is very difficult to optimise the spoilers for both pantograph orientations. Therefore, in recent years, the regulation of air-spring pressure as a function of train speed and pantograph orientation has been proposed as a means to compensate for the aerodynamic uplift and to guarantee the best performances in both running directions and at all speeds [6].

Aerodynamic non-stationary phenomena also influence the performance of a railway pantograph, and can be divided into two groups, related to the turbulence of the incoming flow and to vortex shedding. The presence of recesses, coach separation, electrical insulators, switches and other components installed on the train roof generates a turbulence wake, whose frequency spectrum is likely to excite the pantograph structure also within the frequency range set by international standards for the evaluation of the quality of current collection (0-20 Hz in Europe) [7]. Vortex shedding is generated by collectors of the pantograph head that, due to their rectangular section, can be regarded as bluff bodies [8], [9]. The excitation of these very high frequencies can also affect the quality of current collection, as demonstrated in [10].

This paper proposes a methodology to evaluate the effect that the average drag and lift forces acting on each pantograph part have on the total aerodynamic uplift, not dealing with non-stationary effects.

Aerodynamic uplift needs to be taken into account in pantograph design, in order to minimise its value and its variability in the two orientations in which the pantograph can operate. In this context, the possibility of distinguishing the contribution of each part and the influence of different design solutions to the total aerodynamic uplift is very important. In current design, railway pantographs are based on a one-degree-of-freedom mechanism, named *articulated frame*, which is essentially a

four-bar-linkage. Drag and lift forces acting on pantograph parts tend to open or close the mechanism, and have an influence on the total aerodynamic uplift, depending on the Jacobian terms defining the virtual work that each force is able to produce. The effect of each force to the total aerodynamic uplift can be therefore evaluated through the application of the virtual work principle.

In this work, CFD simulations are validated by means of the comparison with wind tunnel tests, and exploited to evaluate drag and lift forces on pantograph components, to be used as an input for the application of the virtual work principle. The experimental evaluation of these aerodynamic forces is indeed not feasible in operating conditions on a full-scale train, due to the high number of sensors needed, and not advisable in a wind tunnel, due to the several days of testing required when aiming to evaluate different design solutions. CFD simulations, therefore, become a powerful instrument, allowing the identification of the role played by each pantograph component in generating the aerodynamic uplift, and the evaluation of the aerodynamic uplift force corresponding to different pantograph configurations.

The numerical simulation of pantograph aerodynamics has not yet come to maturity, despite the considerable research that has been developed in past years. Experimental on-track tests are still the main instrument not only for the evaluation of pantograph aerodynamic performance during the homologation process, but also for the fine-tuning of the best design solutions. CFD simulations have been performed in literature mainly focusing on the pantograph head (pan-head) and collectors model, in order to study drag and lift forces [7] and acoustic emission [11], [12], [13], [14]. With regard to the possibility of estimating aerodynamic forces on the entire pantograph, some authors have developed CFD models of a full-scale pantograph in a domain representing only the part of the carbody roof close to the pantograph [15], or CFD models of a pantograph installed on a full-scale train [16]. In [5], the authors underline the variability of the aerodynamic uplift force at different heights for both pantograph orientations, but no experimental results are presented. In [17], a full-scale pantograph is tested in a wind tunnel and the experimental results are compared with those of CFD models. In all the mentioned works, however, a complete validation of the CFD model against

experimental results is not available, so that the capability of CFD to reproduce the aerodynamic uplift in an accurate quantitative way has not yet been completely demonstrated [18], [5], [17]. In this paper, the feasibility of using the RANS model is evaluated in order to seek the best trade-off between the achievable results and the computational effort, and to formulate a proposal that is also suitable for industrial applications.

The paper is organised as follows: in section two, experimental wind tunnel tests on a full-scale pantograph are described, and the results of different pantograph configurations are shown. In section three, the CFD modelling is outlined, together with the main modelling features and the results of mesh optimisation. In section four, the model is validated against aerodynamic global forces for all the pantograph configurations tested in the wind tunnel (section 4.1), and thereafter, the procedure for the evaluation of the aerodynamic uplift force based on the virtual work principle and CFD results is described and adopted for all the pantograph configurations tested (section 4.2). Finally, in section five, the analysis focuses on the role played by each pantograph component in generating the aerodynamic uplift.

2. WIND TUNNEL CHARACTERISATION

Wind tunnel tests are a useful tool for a first assessment of the aerodynamic properties of a pantograph. Indeed, they highlight possible criticalities and enable the attainment of indications on the countermeasures needed to achieve the target contact force at every speed with a newly developed pantograph, before aerodynamic on-track tests are carried out. Their drawback consists in the need to reproduce the actual boundary layer of the train roof in order to obtain aerodynamic forces comparable, also quantitatively, to those encountered in operation on a full-scale train. In [19], the authors propose a feasible way to reproduce the full-train boundary layer in a wind tunnel. However, the proposed method still needs experimental on-track tests in order to tune and validate the shape of the obstacles generating the boundary layer. As an alternative, CFD simulations can be used to extend wind tunnel results to the real operating scenario [20]. To this end, it is extremely

important to correctly reproduce the forces acting on the single elements. Wind tunnel results are used therefore, as in this work, for a preliminary investigation of the aerodynamic properties of the high-speed pantograph under analysis, and as a reference to tune and validate the CFD model. The CFD model validated by wind tunnel experiments can then be extended to simulate the full-train scenario, in which the boundary layer of the train roof alters the average aerodynamic forces acting on the lower parts of the pantograph, mainly due to the reduced velocity of the incoming flow.

The wind tunnel tests were performed at the Politecnico di Milano in the high speed, low turbulence test section, whose main characteristics are reported in Table 1. The test section can be used for pantograph applications in either open or closed configuration.

High speed, low turbulence test section		
Section area (wxh)	[m x m]	4x4
Maximum power	[MW]	1.5
Maximum speed	[m/s]	55
Turbulence Intensity I_u	[%]	0.2

Table 1: Main characteristics of the high speed, low turbulence chamber adopted.

For the pantograph used as a reference in this work, the tests were performed in the closed test section, the blockage ratio being around 3%. The pantograph adopted is a modern asymmetrical pantograph, with the lower articulated frame composed of a single cylindrical arm ending with a fork, and the upper part of the articulated frame consisting in a double arm trapezoid. Two independent collectors mounted on cylindrical supports form the pan-head, having pitch degree of freedom with respect to the articulated frame upper bar.

The pantograph was installed in the test chamber on an aluminium structure linked to the ground through a six-component strain gage balance (RUAG 192-6I) placed right below the centre of mass (Figure 1a), so that all the forces and moments exchanged between the pantograph and the ground could be measured. The aluminium supporting structure and the measuring balance were enclosed below a splitter plate (Figure 1b), so as to cut off the boundary layer developing on the floor and place the pantograph in a uniform flow.

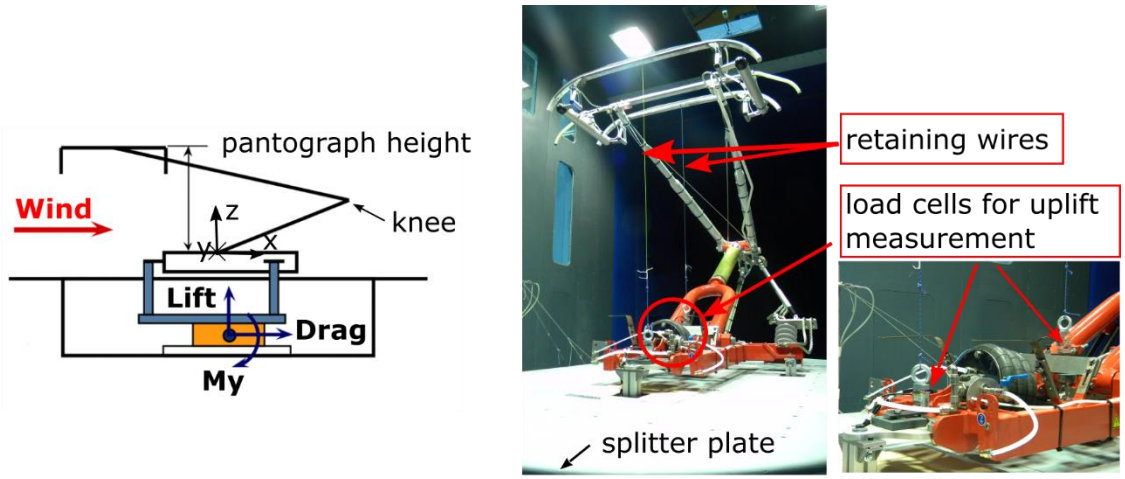

(a) (b)

Figure 1: Pantograph test rig in the wind tunnel. (a) Scheme of the strain-gage balance and supporting structure. According to the wind arrow, the scheme represents the knee-downstream configuration. (b) Test section layout, with the pantograph held by retaining wires.

In pantograph operation, the mean contact force F_m exchanged between pantograph and contact wire is given by the sum of the preload $F_{preload}$ exerted by the pantograph raising mechanism (usually an air-spring), and the aerodynamic uplift F_{uplift}. ($F_m=F_{preload}+F_{uplift}$). The contribution of aerodynamic forces to the mean contact force (aerodynamic uplift) was measured by connecting each pantograph collector, through a retaining wire, to a single axis load cell (DACELL UU-K100) placed at the base of the pantograph fixed frame (Figure 1b). The two cells measure two internal forces, whose sum corresponds to the mean contact force F_m which would be exchanged between the collectors and the contact wire. The aerodynamic uplift was computed for each wind speed as the difference between the total force measured during the tests, due to both the air spring force and the aerodynamic uplift, and the force measured in still air, representing only the air spring uplift contribution.

The aim of the experimental campaign was a preliminary evaluation of the aerodynamic quantities (i.e. aerodynamic uplift, global drag, lift and moment, aerodynamic coefficients, contact force unbalance of the collectors) varying the wind speed, pantograph orientation and working height, deflection of pan-head suspensions. Table 2 summarises all the configurations analysed in the paper, which are described in detail in the following (see also Figure 1, Figure 2 and Figure 4b).

Configuration	**Pantograph orientation** *(see Figure 1a for definition)*	**Pantograph height** *(see Figure 1a for definition)*	**Wind velocity**
Standard pantograph	Knee-upstream and knee-downstream	1.35 m and 1.58 m	33, 38, 44, 50 and 55 m/s.
Pantograph with instrumented pan-head *(see Figure 2)*	Knee-upstream and knee-downstream	1.35 m	33, 38, 44, 50, and 55 m/s.
Pantograph with shielded articulated frame *(see Figure 4b)*	Knee-upstream	1.35 m	33, 38, 44 and 50 m/s.

Table 2: Different pantograph configurations analysed.

All the tests were repeated with different static deflections of the pan-head suspension, obtained with different static preload exerted by the air spring. The results showed that this aspect has no relevant impact on global aerodynamic forces, only affecting the distribution of the mean contact forces between the front and rear collector (contact force unbalance [20]). This aspect is not dealt with in this work.

After testing the standard pantograph, the pantograph head was instrumented with optical load cells, aimed at measuring the force acting through the pan-head suspension, and two optical accelerometers placed on each collector (Figure 2). This set-up, according to EN50317, is used during on-track tests to measure the contact force acting between the collectors and the contact wire. Wind tunnel tests were therefore aimed at identifying the effect of the measurement system on the aerodynamic performances of the pantograph. Figure 2a shows the lay-out of load cells and accelerometers in correspondence of each pan-head suspension, Figure 2b a detail of the standard design of the link between pan-head suspension and collector strip, and Figure 2c a detail of the configuration with load cell and accelerometer. The total height of 0.2 m, indicated in the figure and assumed as the characteristic height of the pan-head, was kept the same for both the standard and the instrumented configuration, thanks to the design of the measuring system.

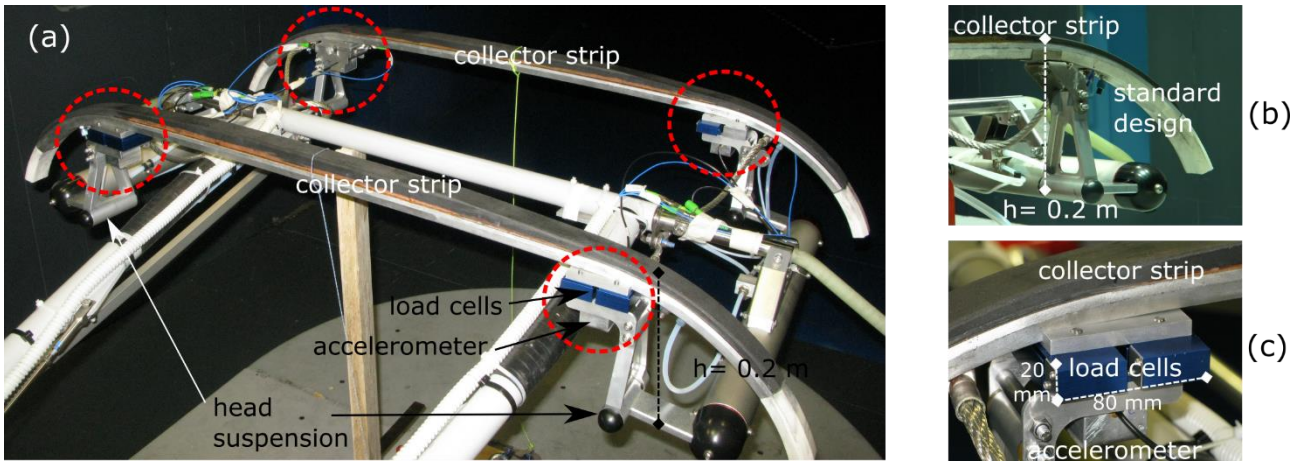

Figure 2: Optical load cells and accelerometers installed on the pantograph for the on-track measurement of contact force (according to EN 50317). (a) Lay-out of pan-head instrumentation. (b) Detail of standard design with no instrumentation. (c) Detail of load cells and accelerometer.

The most relevant issue regarding the analysis of the aerodynamic uplift is the pantograph behaviour corresponding to its two possible orientations, either with the knee upstream or with the knee downstream (see Figure 1a for definition of orientations). Both the orientations were tested at the speeds of 33 m/s, 38 m/s, 44 m/s, 50 m/s and 55 m/s, at two working heights compatible with the actual operating range (i.e. 1.35 m and 1.58 m, measured from the top of the fixed frame to the top of the collectors, as in Figure 1a). The experimental Reynolds number, based on the height of the pan-head (h= 200 mm), ranged from 4.45 x 10^5 to 7.41 x 10^5 (see Figure 2 for the definition of the characteristic length h).

The measuring time of the aerodynamic forces was 40 s, with a sampling frequency of 500 Hz. The data were then averaged to obtain the steady behaviour. Figure 3 reports the total aerodynamic uplift for the standard pantograph with a non-instrumented pan-head, height 1.35 m, both for the orientations with the knee upstream (triangles) and with the knee downstream (squares). As already discussed, the aerodynamic uplift results were obtained by the forces measured in the retaining wires. The corresponding non-dimensional aerodynamic uplift coefficients c_F were evaluated by interpolating the experimental data with a second order polynomial, and adopting the collector width (l=1.3 m) and pan-head height (h= 0.2 m, see Figure 2) to compute the characteristic area $A=lxh$ (ρ=1.22 kg/m^3):

$$c_F = \frac{F_{up}}{\frac{1}{2}\rho V^2 A} \quad (1)$$

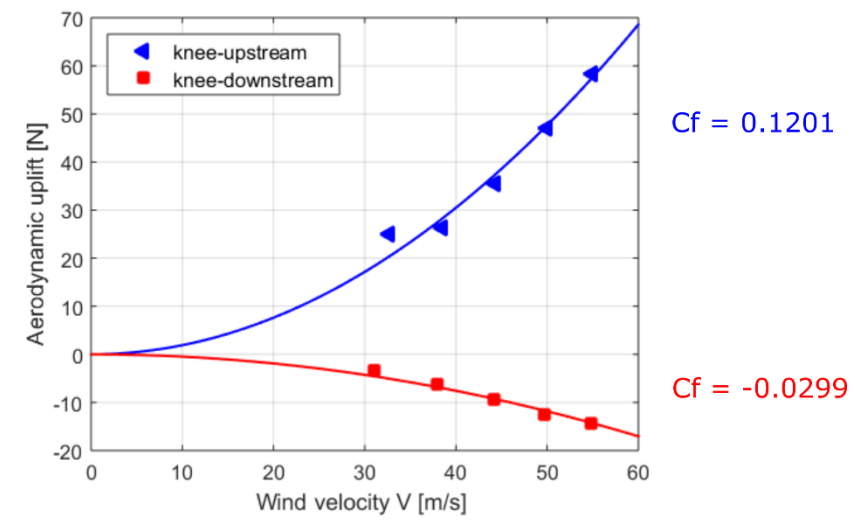

Figure 3: Total aerodynamic uplift. Pantograph working height 1.35 m.

A positive aerodynamic uplift, which would increase the mean contact force, is observed in the case with the knee upstream, and a negative uplift with the knee downstream. Aerodynamic uplifts are not symmetrical, with the positive values higher than the corresponding negative values (e.g. 58 N vs. -15 N for the speed of 55 m/s). Moreover, in the case of knee-upstream (triangles) the forces are very relevant: the experimental tests, carried out up to 55 m/s, show a trend that leads to the prediction of an aerodynamic uplift equal to 130 N at the speed of 83 m/s (300 km/h). This would certainly be critical for the considered pantograph, since the aerodynamic force on its own would be close to the maximum mean contact force prescribed by specifications (e.g. 157 N at 300 km/h according to the Technical Specifications for Interoperability, TSI, 25 kV). This aspect confirms that, when installing the pantograph on a train car-body roof, the need to use shields or shrouds should be considered.

The above results are strongly related to pantograph geometry and kinematics, and can sensibly vary when different pantographs are considered. As an example, the pantograph analysed during the studies reported in [7] shows an opposite trend in a wind tunnel, with a negative aerodynamic uplift in the case of the knee-upstream configuration and a positive aerodynamic uplift in the knee-

downstream case. The pantograph analysed in [17] shows a positive aerodynamic uplift for both orientations.

Furthermore, the non-dimensional uplift coefficients are constant within the speed range tested in the wind tunnel (Figure 3). This result cannot be taken for granted *a priori*, since some of the pantograph components could be sources of speed-dependent aerodynamic behaviour: some literature results [19] have shown pantograph lift coefficients depending on the Reynolds number.

Figure 4a compares the aerodynamic uplift result of the knee-upstream configuration of the standard pantograph (already shown in Figure 3) with the results obtained for the pantograph with an instrumented pan-head, and for the pantograph with an instrumented pan-head and a shield at the bottom of the articulated frame. The shield (see the test configuration represented in Figure 4b) was designed to understand how the presence of the recess area in the car-body roof of the full-scale train could mitigate the significant aerodynamic uplift result highlighted in the knee-upstream configuration.

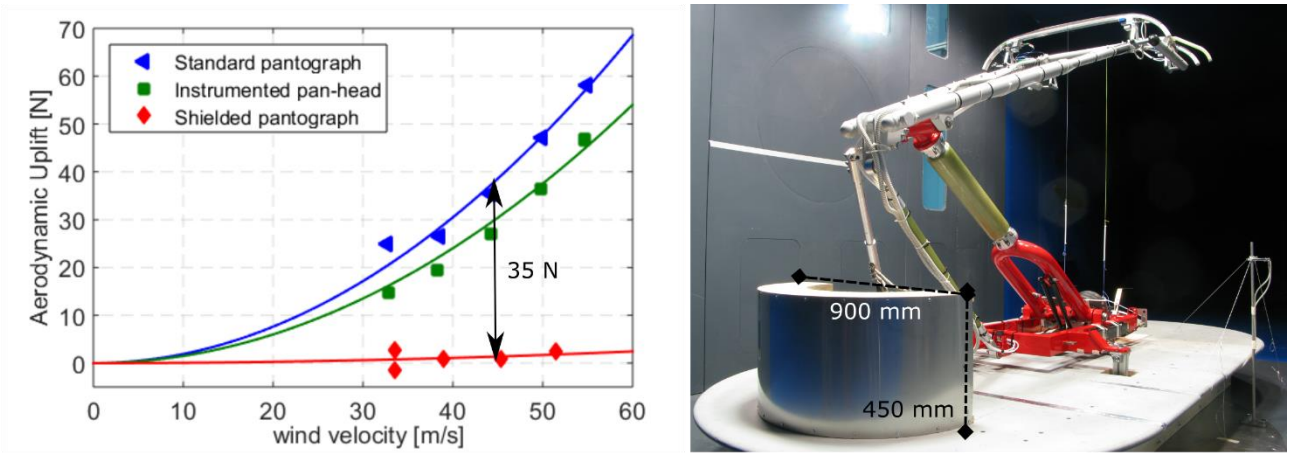

(a) (b)

Figure 4: (a) Total aerodynamic uplift, knee-upstream configuration, working height 1.35 m. Comparison between standard pantograph with non-instrumented pan-head (triangles), pantograph with instrumented pan-head (squares), shielded pantograph with instrumented pan-head (diamonds). (b) Picture of the shielded pantograph.

With respect to the standard pantograph (triangles), a slight reduction of the aerodynamic uplift is obtained in the case of the instrumented pan-head (squares), whereas a sensible decrease can be observed for the shielded pantograph (diamonds), which shows an almost neutral behaviour. It is

worth noting that the global measure of the aerodynamic uplift carried out in the wind tunnel does not enable the discernment of the contribution of the single pantograph components to the global aerodynamic uplift. Nevertheless, the strong variation of the results obtained by shielding the lower part of the articulated frame suggests that the lower arm has a very relevant role in determining the aerodynamic uplift.

Consistent indications are given by the total vertical force *Fz* measured at the strain-gauge balance connecting the pantograph to the ground. The results are reported in Figure 5a: the introduction of pan-head instrumentation (squares) slightly reduces the vertical force, whereas in the case of the shielded pantograph (diamonds) the vertical force dramatically changes and becomes negative. The aerodynamic lift exerted on a skew cylinder is positive when the cylinder is sloping downwards in the wind flow direction, yet negative when it is sloping upwards. Therefore, by shielding the lower arm of the articulated frame in the knee-upstream configuration as in Figure 4b, the positive lift force exerted on that component is partially cancelled and, as far as the articulated frame is concerned, the dominant lift contribution remains the negative one due to the upper arms. It is worth noting that while the presence of the shield generates a strong reduction of the global force *Fz* (-125 N at 45 m/s between the standard and the shielded pantograph), the aerodynamic uplift remains slightly positive, with a reduction of – 35 N at 45 m/s between the standard and the shielded pantograph (Figure 4a, diamond markers). In fact, as discussed hereunder, there is no one-by-one correspondence between the lift forces on pantograph components and the aerodynamic uplift.

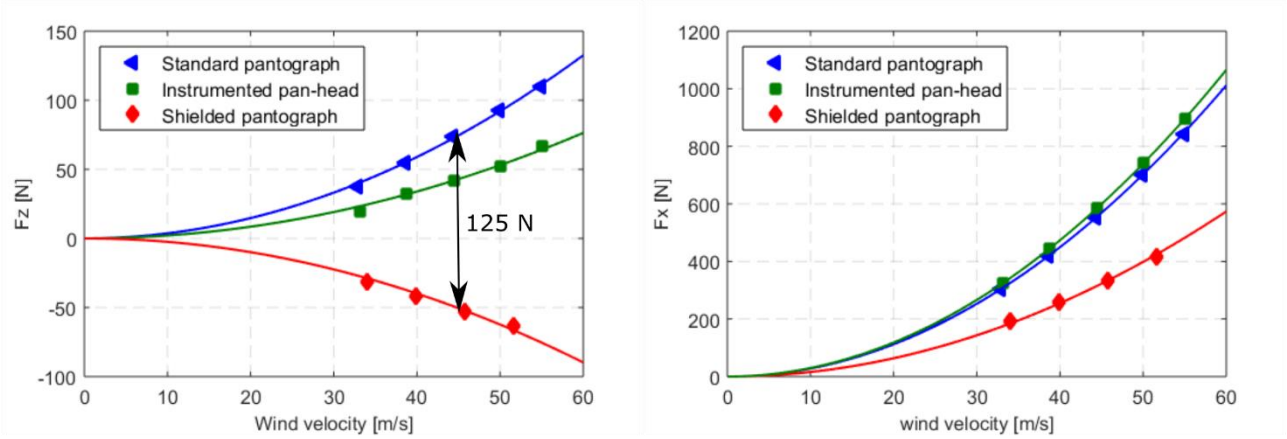

Figure 5: Pantograph height 1.35 m, knee-upstream orientation. Forces measured by the strain gauge balance. (a) Global lift forces (b) Global drag forces.

Figure 5b shows the drag forces measured by the strain gauge balance. Only the knee-upstream results are reported, the drag forces being essentially equal in the two orientations (drag and lift forces for the knee-downstream orientation will be shown hereunder when comparing experimental to CFD results). Once again, the values reported correspond to the standard pantograph (triangles), the pantograph with an instrumented pan-head (squares) and the shielded pantograph (diamonds). As expected, the increase of the frontal section due to the presence of load cells and accelerometers leads to a slight increase of the drag force (+6%). Besides, the shield at the bottom of the articulated frame results in a significant reduction (-40 %) of the drag force.

As for the remaining test configurations, the results obtained for the height of 1.58 m showed an increase in the drag force, due to the greater pantograph frontal area, and low variations of the lift force and aerodynamic uplift.

3. CFD MODELLING

The CFD simulation of a railway pantograph is a complex task, due to the multi-part geometry generating a complex flow around the pantograph, and fluid dynamic interaction between adjacent bodies. Most of the pantograph components are bluff bodies, with a rectangular section in the case of pan-head collectors and with a circular section in the case of the articulated frame's arms. The

297 latter, being inclined cylinders, are very complex to model. For these reasons, the CFD simulation
298 of a railway pantograph requires accurate modelling and good mesh quality.
299 The purpose of the CFD model developed in this paper is the evaluation of the mean drag and lift
300 forces acting on each single part of the pantograph, to be used as input data for a procedure to assess
301 the contribution of each component to the total aerodynamic uplift. This procedure, based on the
302 application of the virtual work principle, is described in the following paragraph 4.2. Experimental
303 wind tunnel results allow the validation of the CFD model in terms of global forces and moments,
304 and the validated model can then be exploited to numerically identify how each pantograph
305 component affects the aerodynamic uplift, and to detect the differences between several pantograph
306 configurations.
307 The modelling choices are subject to contrasting needs, and have to be taken as a trade-off between
308 the achievable results and the cost of the simulations, intended as both hardware resources and
309 computational time. The need to model the forces acting on a complex geometry with several
310 components, bluff bodies and inclined cylinders would lead to approaches such as Detached-Eddy
311 simulation (DES) or Large Eddy Simulation (LES). However, DES simulations require a
312 computational time in the order of weeks [15], even with a High Performance Computing (HPC)
313 external system. They are not, therefore, the best option in a procedure intended to be suitable in
314 industrial contexts, such as pantograph design, planning of experimental tests, and the preliminary
315 assessment of the aerodynamic forces acting on the pantograph. LES simulations for the entire
316 pantograph are not even possible for the time being, and are only possible for a part of it [12]. On
317 the other hand, Reynolds-Averaged Navier-Stokes (RANS) solutions, although less accurate in
318 predicting the forces acting on the single parts [21], allow a sharp decrease in computational time,
319 and can therefore be a suitable solution for a first assessment of each pantograph component's
320 weight on the aerodynamic uplift, especially during the design process.
321 Steady-state RANS simulations were adopted with the aim of verifying the suitability of the RANS
322 approach for the purpose of this work, i.e. the evaluation of each pantograph component's weight to

the total aerodynamic uplift. Steady-state simulations are considered an adequate choice, since experimental global forces showed limited fluctuations. The maximum ratio between the standard deviation and the average force in experimental data is equal to 4% (less than 1.5% in most cases). Simulations were performed in a few hours (from 4 to 9 hours) on an HPC system (72 CPUs) and, therefore, the model could be effectively applied to the analysis of several variants and configurations of the same model, as required for pantograph orientations and working heights.

Steady RANS simulations were carried out with the Open-Source code *Open Foam*, which is a code based on the Finite Volume Method. The turbulence model adopted is the *k-ω SST*, which presents a good behaviour in the presence of adverse pressure gradients and flux separation [22], largely occurring on various pantograph components such as cylinder and bluff bodies.

Figure 6 represents the computational domain used for simulating the wind tunnel tests, while Table 3 encompasses the boundary conditions adopted.

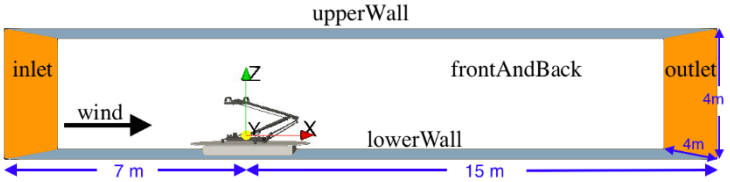

Figure 6: Computational domain for simulating the wind tunnel tests.

Boundary conditions		
Patch Name	**p**	**U**
Inlet	$\nabla p = 0$	U_∞
Outlet	0	$\nabla U = 0$
Lower wall	$\nabla p = 0$	0
Upper wall	Symmetry plane	
Front and Back	Symmetry plane	
Pantograph surfaces	$\nabla p = 0$	0
Splitter plate	$\nabla p = 0$	0

Table 3: Boundary conditions adopted for the CFD simulation (pressure p and velocity U)

The mesh was built with the mesh generation utility *snappyHexMesh*, supplied with *OpenFOAM*, which creates 3-D unstructured grids starting from a perfectly structured grid (Hexahedra). The mesh refinement was carried out through subsequent mesh and simulation steps, so as to obtain the convergence of the solution with as dense a mesh as necessary. Grid independence on pantograph

forces was studied with different refining levels, corresponding to the total amount of 6, 10 and 13 million cells. The most relevant result of this process was the ascertainment of the numerical results' significant sensitivity to the presence of cell layers close to pantograph surfaces, which need to have high regularity to get accurate results (see Figure 7d and Figure 8a). When the layers are not present, or their coverage on the pantograph is not uniform, the force and moment results are rather inaccurate and are unable to yield the trends occurring for different test configurations. The final 20 million cell mesh was obtained as the result of the presence of one or two layers close to the walls of the pantograph components. No relevant differences were obtained by using a 30 million cell mesh, obtained by extending the zone with thick mesh in the proximity of the pantograph components. Figure 7 shows the mesh refinement levels of the entire domain, and the average dimension of the cells in each level (Figure 7a knee-upstream case, Figure 7b knee-downstream case). For both orientations, the pantograph's origin is set at 7 m from the inlet and at 15 m from the outlet, for a correct development of the wind wake behind the pantograph. Figure 7c shows an enlargement of the mesh refinements adopted in the proximity of the pantograph, Figure 7d is an example of mesh in the proximity of pantograph surfaces, with pantograph layers visible at level 6.

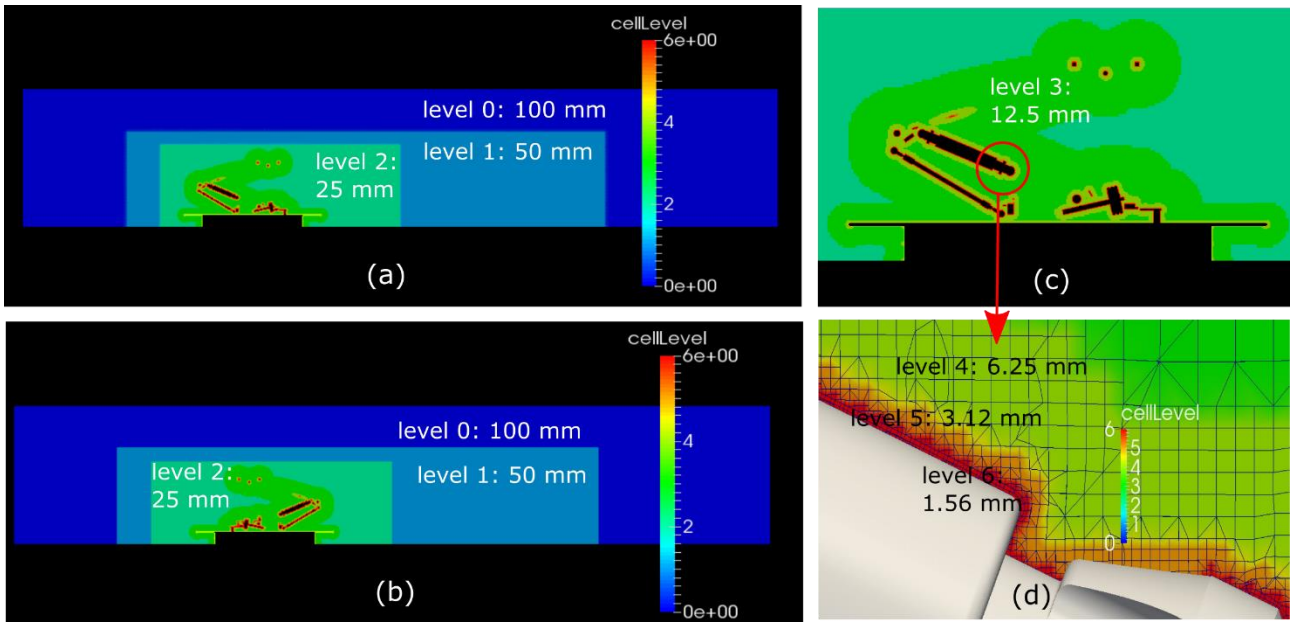

Figure 7: Mesh refinement levels. (a) Entire domain, knee-upstream. (b) Entire domain, knee-downstream. (c) Cell levels in proximity of the pantograph. (d) Detail of pantograph lower arm.

Even if the *k-ω SST* model can also be used without wall functions within the fine mesh close to the solid surfaces of the pantograph, the use of wall functions was preferred to contain the computational effort and to benefit industrial applicability. In principle, the use of wall functions to describe the speed profiles in proximity of the solid surfaces is not preferable when modelling cylindrical geometries ([23], [24]) since it leads to an underestimation of the aerodynamic coefficients. Nevertheless, for pantograph applications, the forces generated on the components composing the articulated frame are significantly affected by the geometries connected to the extremities of the skewed cylinders, (e.g. the revolute joints and the fork visible in Figure 4b), so that the use of wall functions does introduce an acceptable error. The two approaches (use of wall functions and $y^+ \approx 50$ *vs.* direct solution of the boundary layer and $y^+ \approx 1$) were initially compared by simulating a single arm of the pantograph, and the differences in results were limited to 10-20%, with lower force results obtained by using wall functions. The increase of cells needed to get $y^+ \approx 1$ on a single pantograph arm was very significant, i.e. 11 million instead of 4 million when wall functions are used. In the complete pantograph case, therefore, the boundary layer was not solved, but modelled with wall functions. The average y+ values obtained in correspondence of the main pantograph surfaces varied between 48 and 78 (for the simulation at 40 m/s), in agreement with the requirements of the wall functions used (*nutkWallFunction*). Higher y+ values (average value 214) were adopted for the splitter plate wall, where a coarser mesh can be used. Figure 8a gives an overview of the percentage of the pantograph surfaces covered by cell layers in the final mesh, while Figure 8b shows an example of y+ values obtained. Details of the final mesh are given in Table 4.

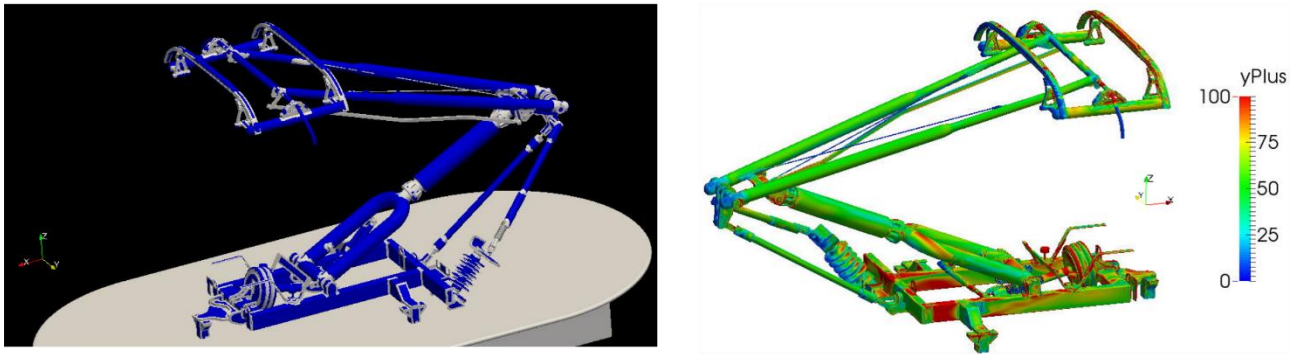

(a) (b)

Figure 8: Details of pantograph mesh and simulation results. (a) Pantograph surfaces covered by layers. (b) Example of y+ on pantograph surfaces, simulation 40 m/s, Knee-upstream. Height 1.35 m

Cell count	~20 million
Element types	Hexahedra (86%)
Minimum Refinement level	Level 0 Mean cell dimension 100 mm
Maximum Refinement level	Level 6 Mean cell dimension 1.56 mm
Surface Layers	1 or 2 layers on pantograph components
Mesh quality	Maximum aspect ratio 32.8
	Average non-orthogonality 9.7
	Maximum non orthogonality 74 (10 faces)
	39 faces with skewness > 4 (Max 9.6)

Table 4: Details of the mesh.

The *SimpleFoam* solver, which is based on the standard SIMPLE algorithm, was used. Table 5 reports the main modelling features. Convergence was evaluated by considering both residuals and force coefficients. Two thousand iterations were performed for each simulation, and stable results for residuals were achieved after about five hundred iterations.

Simulation approach		Steady RANS
Turbulence model		k-ω SST
Solver Algorithm		SIMPLE
Gradient Discretisation scheme		Gauss Linear
Divergence Discretisation scheme	U	Gauss Linear Upwind
	k	Gauss upwind
	ω	Gauss upwind

Table 5: Main modelling features.

4. MODEL VALIDATION

4.1. CFD validation against strain-gauge balance forces and moments

The global forces and moments measured by the strain-gauge balance, even if not directly affecting the quality of current collection, are of relevant interest in the procedure proposed in this work, since they can be used to validate the numerical results obtained by CFD analysis.

Figure 9, Figure 10 and Figure 11 report the comparisons between numerical and experimental forces and moments, for both the knee-upstream and knee-downstream configurations and the heights of 1.35 m and 1.58 m. With reference to the coordinate system of Figure 1a and Figure 6, attention is focused on drag force (Fx), lift force (Fz), and pitch moment (My).

Figure 9 shows the drag force Fx for knee-upstream (a) and knee-downstream (b) orientations. For the sake of clarity, the set of results has not been wholly reported. For the knee-upstream case, the height of 1.35 m is considered together with the drag forces corresponding to the standard pantograph (triangle), the pantograph with an instrumented pan-head (square), and the shielded pantograph (diamond). The experimental results are represented with filled markers in the figures, and the CFD results with empty markers. For the knee-downstream case (Figure 9b), the results corresponding to the standard pantograph are compared for the height of 1.35 m and 1.58 m. Table 6 reports the evaluated drag coefficients, based on the interpolating second order curve for all the configurations tested.

The numerical drag results are sufficiently accurate. They are able to catch the drag increase due to the presence of pan-head instrumentation (Figure 9a and Table 6), the significant drag decrease due to the shield effect (Figure 9a and Table 6), and the slight drag increase corresponding to the higher height of 1.58 m (Figure 9b and Table 6), in which the pantograph frontal section exposed to the flux is increased. The maximum errors between numerical and experimental drag results for the knee-upstream orientation are 5.3% for the standard pantograph, 5.1% for the shielded pantograph, and 4.9% for the instrumented pantograph. As for the knee-downstream orientation, the error for the standard pantograph case is 1.9% for the height of 1.35 m, and 1.6% for the height of 1.58 m. The

error is equal to -2.9% for the instrumented pantograph, knee-downstream orientation, whose results are not reported in the figure.

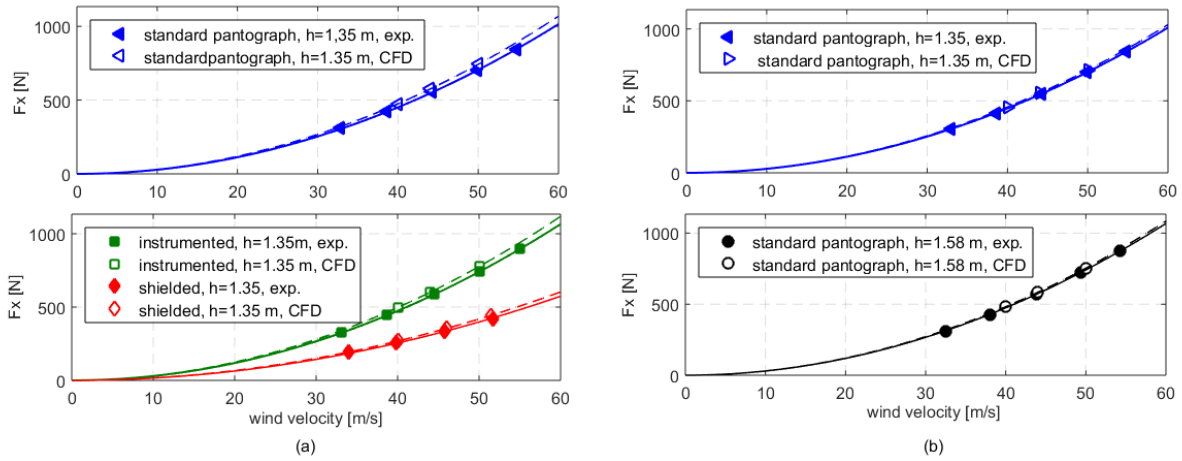

Figure 9: Drag force Fx. Numerical and experimental results. (a) Knee-upstream. (b) Knee-downstream.

Drag coefficients $c_D = \frac{F_x}{\frac{1}{2}\rho V^2 A}$, $A = w \times l$, *w=0.2 m, l=1.3 m*						
Pantograph configuration	**Knee-upstream**			**Knee-downstream**		
	Experimental	**CFD**	**Error [%]**	**Experimental**	**CFD**	**Error [%]**
Standard, h 1.35 m	1.778	1.872	+5.3 %	1.769	1.803	+1.9 %
Standard, h 1.58 m	1.854	1.952	+5.3%	1.870	1.9	+1.6 %
Instrumented, h 1.35 m	1.866	1.959	+4.9 %	1.894	1.839	-2.9 %
Shielded, h 1.35 m	1.005	1.056	+5.1 %	-	-	-

Table 6: Comparison between experimental and CFD drag coefficients (C_D).

Figure 10 reports the total lift force F_z, measured and evaluated by CFD. The corresponding lift coefficients C_L are reported in Table 7. Also in this case, the knee-upstream simulation results (Figure 10a) can get the trends of experimental data corresponding to different pantograph configurations. CFD results correctly reproduce the lift force in the standard pantograph, knee-upstream case (error 5.3%), the decrease of lift force due to the presence of the pan-head instrumentation, and the drastic decrease due to the shield at the bottom of the articulated frame. Some discrepancies are obtained for the knee-downstream configuration. Figure 10b shows the results related to the different working heights for the standard pantograph, in which the numerical results over-estimate the experimental ones. The error between CFD and experimental lift

coefficients is 161% for the height of 1.35 m and 181% for the height of 1.58 m, corresponding respectively to 43 N and 46 N at the velocity of 55 m/s. The origin of this lack of accuracy in the knee-downstream orientation is likely to be a model shortcoming in representing the turbulent wake generated by the air spring at the base of the articulated frame, and its interaction with the lower parts of the pantograph in the knee-downstream case (see section 5). This hypothesis is corroborated by the analysis of lift forces on each pantograph component. The lift contributions of the pan-head and the upper arms of the articulated frame are consistent in the two orientations, with knee-upstream and knee-downstream orientation, as will be shown hereunder (see section 5, Figure 14). On the contrary, the lift forces introduced by the lower arm of the articulated frame and by the fixed frame are significantly different. The origin of lift surplus in the knee-downstream simulation must therefore be identified in the simulation forces on these components, arising from the interaction with a turbulent wake. In this condition, CFD results are less accurate. However, it is worth remarking that the fixed frame contribution does not influence the aerodynamic uplift, and the incident flow on the lower parts of the pantograph in real operation is very limited due to the train-roof boundary layer, as shown in [20].

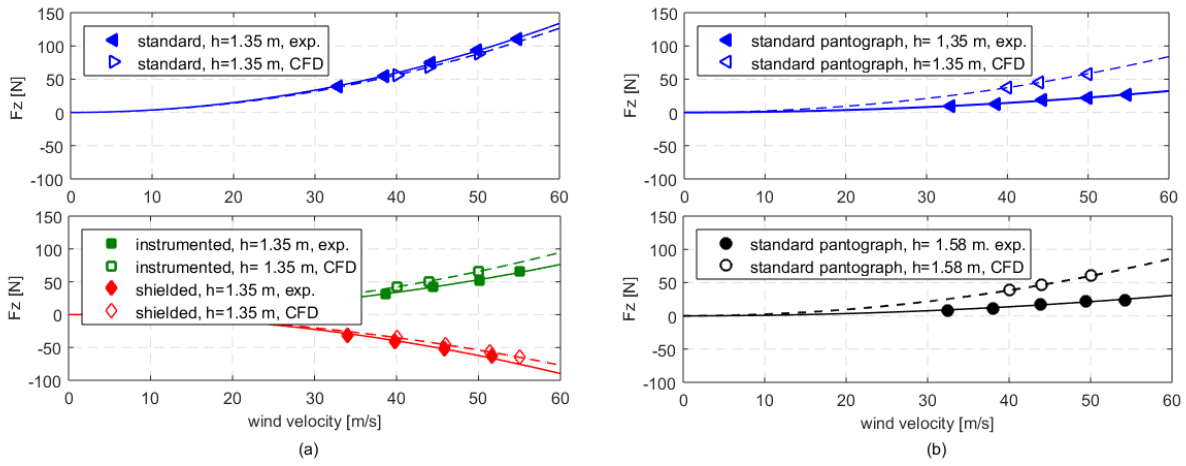

Figure 10: Lift force Fz. Numerical and experimental results. (a) Knee-upstream. (b) Knee-downstream.

Lift coefficients $c_L = \frac{F_z}{\frac{1}{2}\rho V^2 A}$, $A = w \text{ x } l$, *w=0.2 m, l=1.3 m*						
Pantograph configuration	**Knee-upstream**			**Knee-downstream**		
	Experimental	**CFD**	**Error [%]**	**Experimental**	**CFD**	**Error [%]**
Standard, h 1.35 m	0.235	0.222	-5.4 %	0.056	0.147	43 N@55m/s 161 %
Standard, h 1.58 m	0.213	0.209	-2.1 %	0.054	0.151	46 N@55m/s 181 %
Instrumented, h 1.35 m	0.134	0.166	+ 24.0 %	0.096	0.097	1 %
Shielded, h 1.35 m	-0.157	-0.135	-14.2 %	-	-	-

Table 7: Comparison between experimental and CFD lift coefficients (C_L).

Finally, the pitch moment My is reported in Figure 11, and the corresponding aerodynamic moments coefficients C_{My} in Table 8. The numerical results correlate with the experimental ones, allowing a validation of the numerical model. With reference to Figure 11a (knee-upstream orientation), the error between experimental and CFD moment coefficients is equal to -13% for the standard pantograph, -8.8 % for the instrumented pantograph, and -3.4% for the shielded pantograph. As in the case of the lift force, the results related to the knee-downstream orientation are less accurate, both for the standard and for the instrumented pantograph, being the maximum error equal to -29.9% for the standard pantograph and -32% for the instrumented pantograph. Nevertheless, as shown in Table 8, also in this orientation the model is able to catch the trends corresponding to different heights and the presence of pan-head instrumentation.

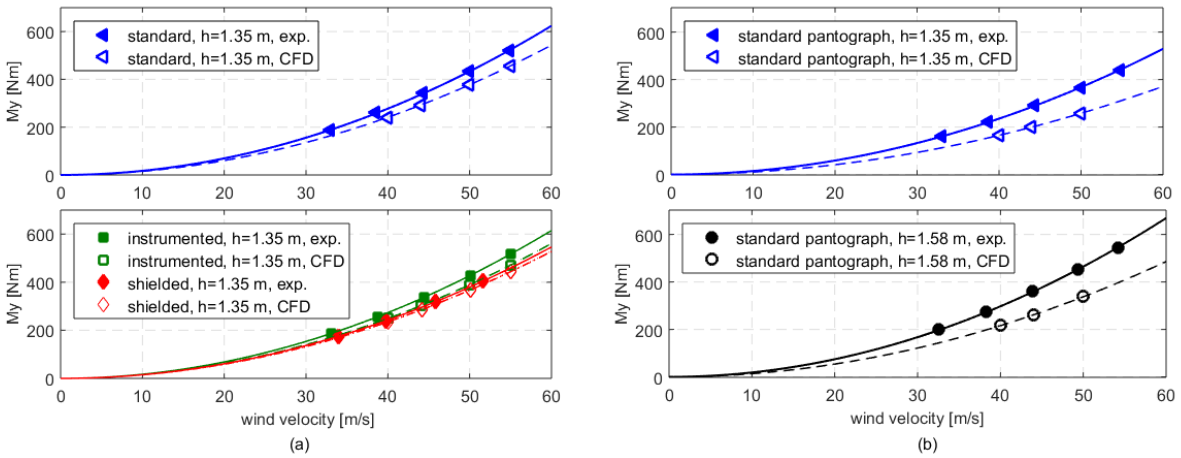

Figure 11: Pitch moment My. Numerical and experimental results. (a) Knee-upstream. (b) Knee-downstream.

My pitch moment coefficients $c_{My} = \frac{M_y}{\frac{1}{2}\rho V^2 A l}$, $A = w \text{ x } l$, *w=0.2 m, l=1.3 m*						
Pantograph configuration	**Knee-upstream**			**Knee-downstream**		
	Experimental	**CFD**	**Error [%]**	**Experimental**	**CFD**	**Error [%]**
Standard, h 1.35 m	0.841	0.732	-13%	0.713	0.500	-29.9%
Standard, h 1.58 m	1.000	0.881	-12%	0.902	0.655	-27.4%
Instrumented, h 1.35 m	0.829	0.756	-8.8%	0.773	0.526	-32%
Shielded, h 1.35 m	0.736	0.711	-3.4%	-	-	-

Table 8: Comparison between experimental and CFD pitch moment coefficients (C_{My}). The distance *l* adopted is the collector width *l*=1.3 m.

4.2. CFD validation against aerodynamic uplift force

CFD simulations allow the calculation of the aerodynamic forces and moments acting on each single component of the pantograph, but do not allow the direct computation of the resulting aerodynamic uplift. From a mechanical point of view, the aerodynamic uplift corresponds to the Lagrangian component of all the aerodynamic forces over the pan-head displacement, and cannot therefore be directly estimated from the CFD model, in which the pantograph is regarded as a rigid body and the kinematic links are not taken into account. A procedure for the estimation of the aerodynamic uplift force from the aerodynamics forces on single pantograph parts was described and validated in [20]. It is based on the forces resulting from the CFD simulation of the pantograph, and the Jacobian terms calculated from the kinematic analysis.

In the virtual work principle equation (2), the virtual work done by all the drag ($F_{x,i}$) and lift ($F_{z,i}$) forces acting on each i-th component of the pantograph is equal to the virtual work of the aerodynamic uplift F_{uplift}.

$$\sum_i F_{x_i} \delta x_i + \sum_i F_{z_i} \delta z_i = F_{Uplift} \delta z_h \quad (2)$$

All the forces $F_{x,i}$ and $F_{z,i}$ are obtained from CFD simulations. The Jacobian terms, relating the virtual vertical displacement of the pan-head (δz_h) to the virtual horizontal (δx_i) and vertical (δz_i) displacements of the application points of the aerodynamic forces are calculated by considering the pantograph as a single degree of freedom system, based on the four bar linkage of the articulated frame.

Figure 12 reports a scheme of the kinematic model (Figure 12a) and a scheme of all the forces considered in the aerodynamic uplift computation (Figure 12b).

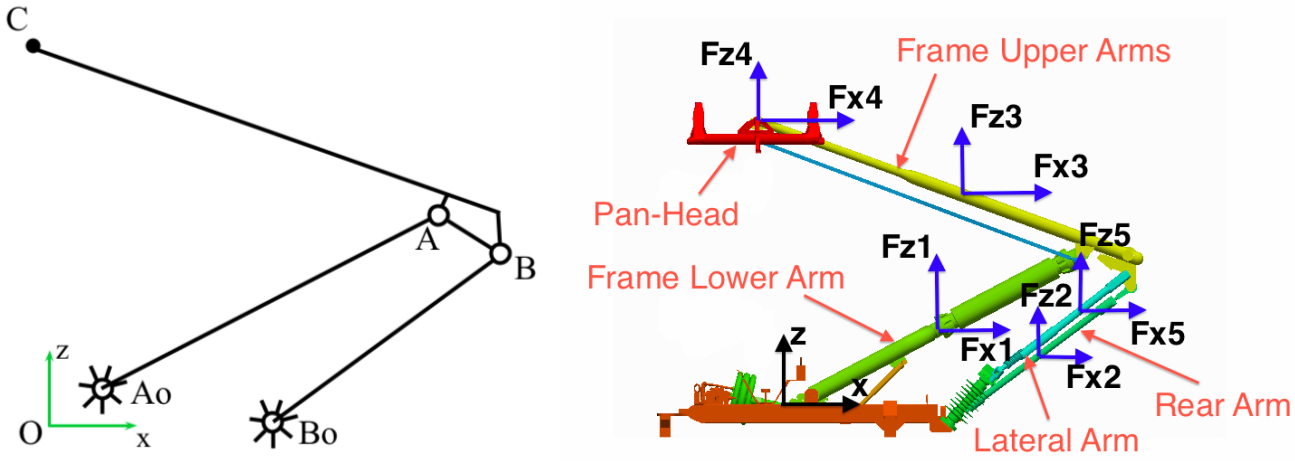

Figure 12: Pantograph kinematic scheme. (a) Articulated frame as a four bar linkage. (b) Forces taken into account for the aerodynamic uplift computation.

The estimation of the aerodynamic uplift obtained by the method summarised above and fully described in [20] can be considered very satisfying: Figure 13 compares the experimental wind tunnel results with the corresponding numerical results, for both the pantograph orientations and heights. Figure 13a refers to the knee-upstream orientation and Figure 13b to the knee-downstream orientation. Table 9 reports the aerodynamic uplift coefficients for all the configurations tested.

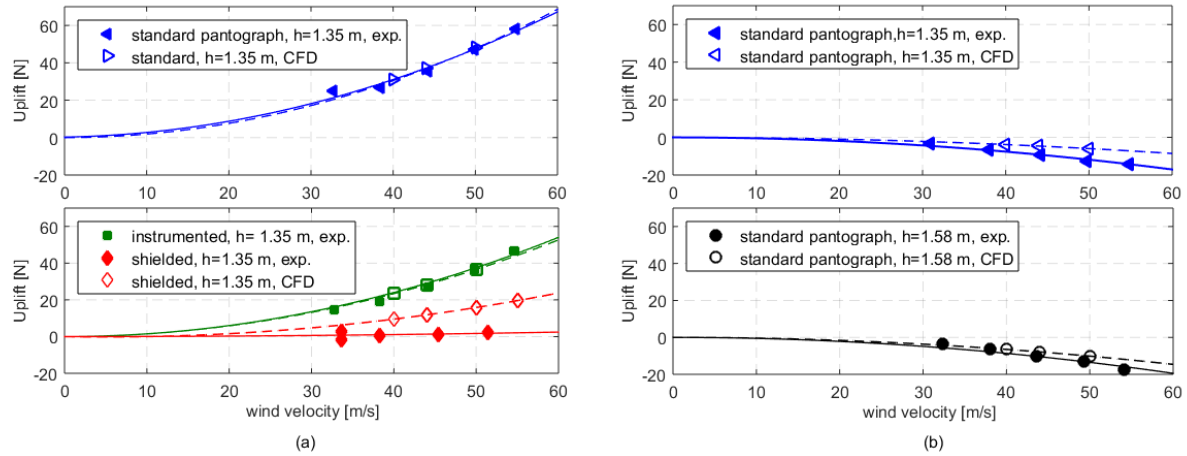

Figure 13: Pantograph aerodynamic uplift: comparison of numerical and experimental results. (a) knee-upstream pantograph, height 1.35 m. (b) knee-downstream standard pantograph, height 1.35 m and 1.58 m.

Aerodynamic uplift coefficients $c_F = \frac{F_{up}}{\frac{1}{2}\rho V^2 A}$, $A = w \text{ x } l$, *w=0.2 m, l=1.3 m*						
Pantograph configuration	**Knee-upstream**			**Knee-downstream**		
	Experimental	**CFD**	**Error**	**Experimental**	**CFD**	**Error**
Standard, h 1.35 m	0.120	0.118	-1.9 %	-0.030	-0.015	-7 N @55m/s 49.8 %
Standard, h 1.58 m	0.118	0.117	-0.6 %	-0.034	-0.026	-4 N @55m/s -24.9 %
Instrumented, h 1.35 m	0.095	0.092	-2.6 %	-0.033	-0.043	-5 N @55m/s (28.7%)
Shielded, h 1.35 m	0.004	0.042	+18N @55m/s	-	-	-

Table 9: Comparison between experimental and CFD aerodynamic uplift coefficients (C_F). The adopted length *l* is the collector width *l*=1.3 m.

The model can correctly reproduce the trend of the aerodynamic uplift force corresponding to different test conditions, with the most significant error in the case of the shielded pantograph. With reference to the knee-upstream orientation (Figure 13a), the error between experimental and numerical aerodynamic uplift coefficients is -1.9% for the case of the standard pantograph (triangles) and -2.6% for the case of the pantograph with an instrumented pan-head (squares), which shows a reduction of the aerodynamic uplift. A slightly positive aerodynamic uplift is numerically estimated for the shielded pantograph (diamonds), whereas the corresponding experimental results show an almost null aerodynamic uplift (error 18 N at 55 m/s). For the knee-downstream case of Figure 13b, the results referring to two different heights of the standard pantograph are reported (1.35 m and 1.58 m). The trend shows a slight increase of the down-lift force corresponding to the higher pantograph height and is properly captured by numerical results, even if with an underestimation (almost negligible) of the force magnitude.

The results reported in paragraph 4.1 and paragraph 4.2 lead to the conclusion that the developed model, based on the RANS equations, is able to obtain the trend corresponding to different pantograph configurations. The procedure, consisting in CFD simulations and the application of the virtual work principle can, therefore, be used as a tool in pantograph design, to be exploited to develop solutions with a small aerodynamic uplift in which the contact force is as neutral as possible to aerodynamic forces.

5. ROLE OF PANTOGRAPH COMPONENTS IN GENERATING AERODYNAMIC UPLIFT

Figure 14 reports the forces obtained on each single component of the pantograph for the CFD simulation case corresponding to the standard non-instrumented pantograph with a height of 1.35 m. Figure 14a refers to knee-upstream while Figure 14b refers to knee-downstream orientation. When comparing the two orientations, the most significant difference in the aerodynamic forces on the pantograph parts is the lift force component on the lower arm.

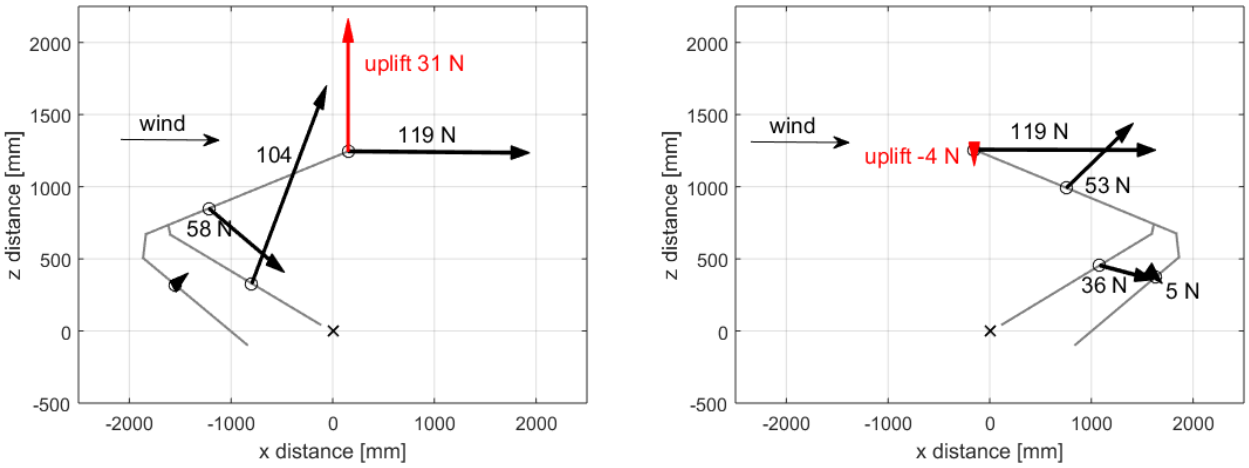

Figure 14: CFD forces on pantograph components, wind velocity 40 m/s, standard pantograph, height of 1.35 m. (a) Knee-upstream. (b) Knee-downstream.

This force appears to be the most relevant reason for the asymmetry experimentally observed in the aerodynamic uplifts corresponding to the two orientations (see Figure 3 and Figure 13). Moreover, the high magnitude of the force (Figure 14a, 104 N) explains why the aerodynamic uplift is strongly decreased by shielding the lower part of the articulated frame in the knee-upstream orientation (Figure 13a).

A deeper investigation of the reason for the different forces acting on the lower arm of the articulated frame can be found by looking at the air flow. Figure 15 reports the velocity field (magnitude) and the kinetic energy K for both the knee-upstream and knee-downstream orientation. The images refer to a cutting plane passing through the middle of the pantograph (see dashed line in Figure 16), and therefore the fork of the lower arm and the upper arms of the articulated frame are not visible. The fork is reported in transparency in Figure 15 and is indicated with an arrow. The

main differences in the wind flow blowing over pantograph components can be observed in the stream around the lower arm of the articulated frame. In the knee-upstream case (Figure 15a and Figure 15c) an unperturbed flow impacts on the pantograph's articulated frame, whereas in the knee-downstream case (Figure 15b and Figure 15d) a shielding effect is created by the air spring (highlighted in the figure), which generates some turbulence in the flow interacting with the lower arm. Consequently, the force acting on the lower arm in the knee-downstream case is lower in magnitude, and the application point of the force is moved upward with respect to the knee-upstream case.

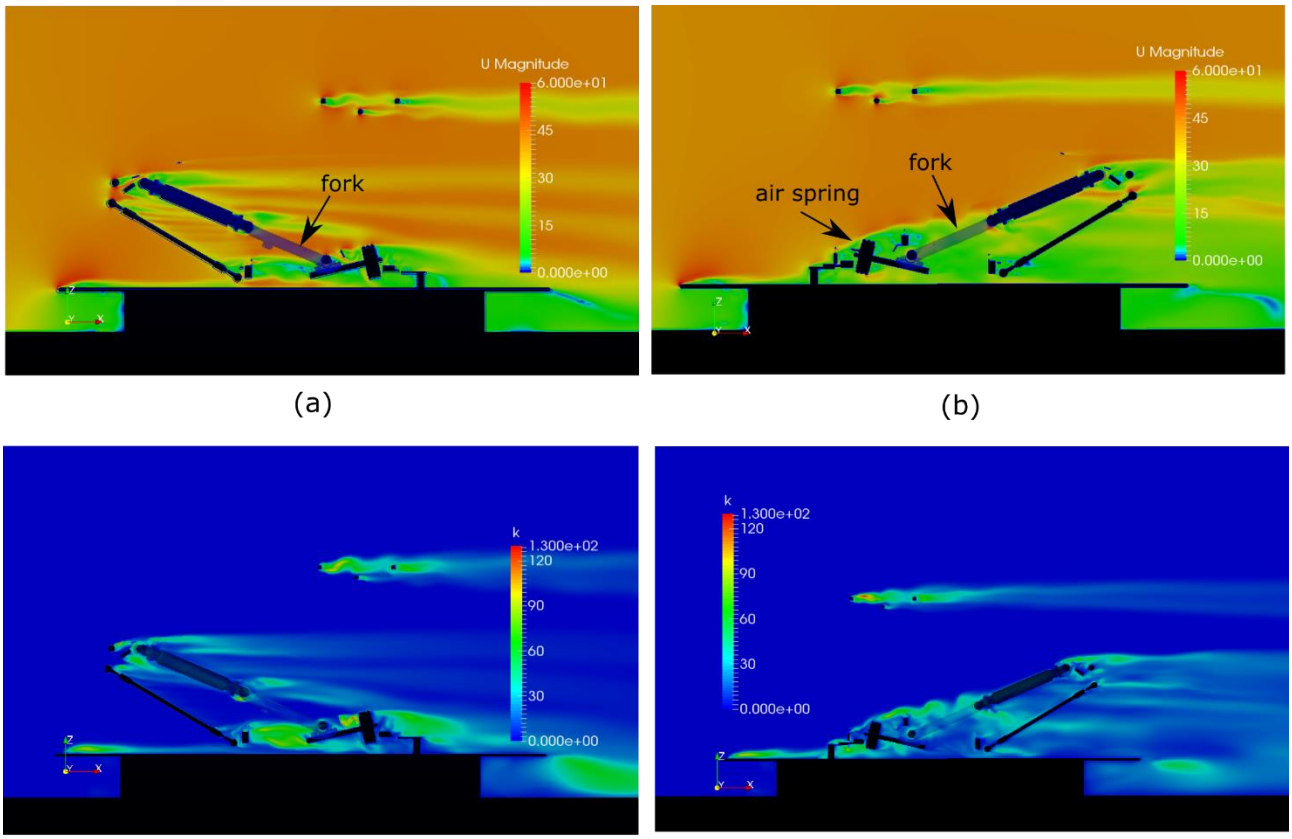

Figure 15: Velocity fields (magnitude) and Kinetic Energy *K* of the simulations of the pantograph in the wind tunnel. Wind velocity 40 m/s, standard pantograph, height of 1.35 m. (a) knee-upstream, velocity. (b) knee-downstream, velocity. (c) Knee-upstream, *K*. (d) Knee-downstream, *K*.

The shielding effect generated by the air spring is also clearly visible by looking at the static pressures on the pantograph components. Figure 16 reports the pressure values. Figure 16a refers to the knee-upstream while Figure 16b refers to the knee-downstream orientation. The maximum

pressure detected on the lower arm fork is 1037 Pa for the knee-upstream case (Figure 16a), and 549 Pa for the knee-downstream case (Figure 16b).

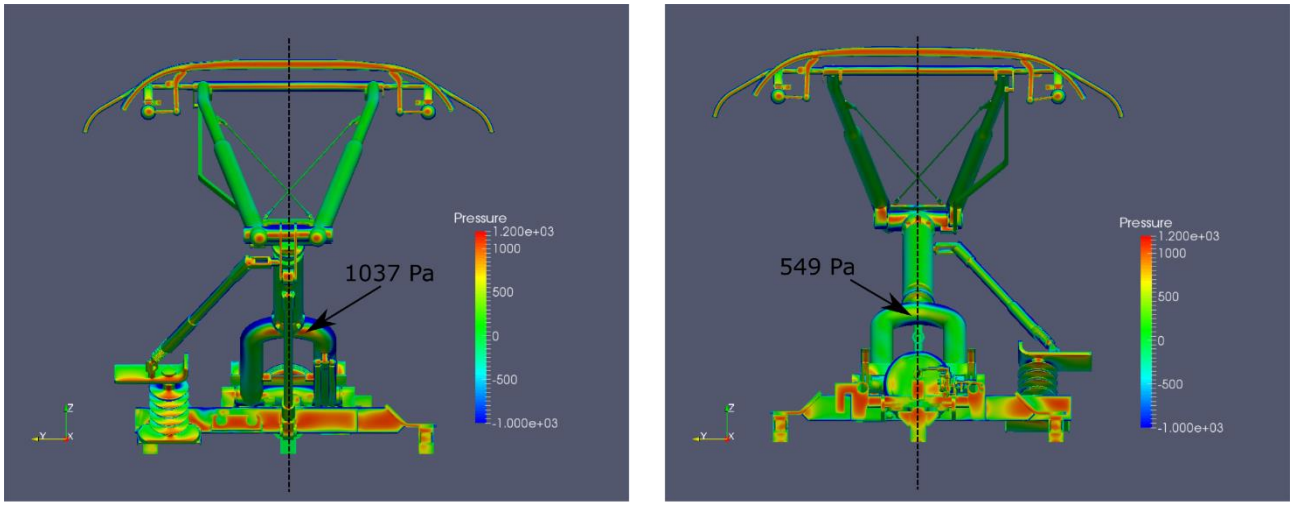

Figure 16: Pressures on pantograph components. (a) knee-upstream orientation. (b) Knee-downstream orientation.

As already mentioned, the definition of the forces acting on the pantograph is not sufficient to assess the contribution of each component to the total aerodynamic uplift. In fact, the role played by each part is determined not only by the force magnitudes and directions, but also by the Jacobian terms defining the virtual work that each force is able to produce. Due to the x-direction component of each virtual displacement, also drag forces can have a remarkable impact on the aerodynamic uplift.

The bar diagram in Figure 17 represents, for each i-th pantograph component labelled in Figure 12b, the contributions to the global aerodynamic uplift due to the drag force (white bars) and to the lift force (grey bars), representing respectively the terms $Fx_i \frac{\delta x_i}{\delta z_h}$ and $Fz_i \frac{\delta z_i}{\delta z_h}$ in the summation of the equation (2). In addition, the black bars represent the aerodynamic uplift contribution due to the total force (sum of drag and lift components). The reported results refer to the non-instrumented standard pantograph, height of 1.35m and wind velocity of 40 m/s. The value of the total aerodynamic uplift (from CFD) is reported with the dashed line, in order to show the weight of each component in generating the total aerodynamic uplift.

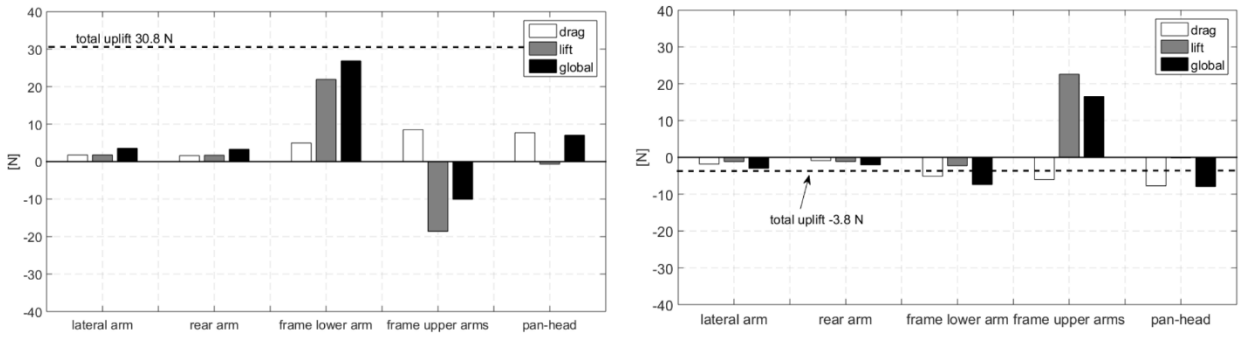

Figure 17: Analysis of the contribution of each component of the pantograph to the total uplift force (standard pantograph, height of 1.35 m, wind velocity of 40 m/s). (a) Knee-upstream. (b) Knee downstream.

Due to the kinematic relationships, all the drag forces tend to open the pantograph and to increase the aerodynamic uplift in the case of knee-upstream orientation (Figure 17a), and they show the opposite behaviour for the knee-downstream orientations (Figure 17b), tending to close the pantograph and giving a negative contribution to the aerodynamic uplift. It is worth stating that the contribution of the pan-head to the total aerodynamic uplift (last bar on the right of each figure) is quite relevant, even if the force acting on the pantograph head is essentially drag force, as already pointed out in Figure 14. This is because the Jacobian term $\frac{\partial x_h}{\partial z_h}$ (indicating the horizontal displacement of the pan-head δx_h corresponding to a vertical displacement δz_h) is non-null. The Jacobian terms, therefore, play a role as important as the forces on the pantograph components in generating the aerodynamic uplift. The pan-head's role that emerges from this analysis is, however, less dominant than in [25], where it is indicated as the component that mainly determines the pantograph's aerodynamic performance. Another difference with the results of [25] is related to the flow's angle of attack on the pan-head in the knee-upstream orientation. In [25] the authors state that, for this orientation, the upper arms deviate the flow upwards, thus inducing a high effective angle of attack with respect to the pan-head. To the contrary, the results of the CFD simulations performed in this work showed a non-relevant deviation of the flow due to the articulated frame's upper arms, and the same angle of attack on the pan-head for both the knee-upstream and knee

downstream orientations. This is consistent with the fact that the force acting on the pan-head does not change in the two orientations, and has no relevant lift component (see Figure 14).

Figure 18 compares the contributions to the aerodynamic uplift considering the instrumented pan-head (Figure 18a) and the shield at the bottom of the articulated frame (Figure 18b). The results refer to the pantograph height of 1.35 m at 40 m/s, knee-upstream orientation, and can therefore be compared to the results of Figure 17a, referring to the standard pantograph. The presence of the instrumentation mounted on the pan-head generates a negative lift force, which adds to the aerodynamic uplift contribution due to the drag force, already discussed in the standard pantograph case. This results in an almost null aerodynamic uplift contribution generated by the pantograph head, which is the reason why the experimental and numerical total aerodynamic uplift is lower in the case of the instrumented pantograph than in the case of the standard pantograph (see Figure 13a).

By comparing the aerodynamic uplifts generated in the presence and absence of the shield at the bottom of the articulated frame (Figure 18b against Figure 18a), it is clearly visible that the shield's presence reduces the lower arm's contribution to the total aerodynamic uplift, mainly due to the reduction of its lift force. This shielding effect can be achieved in the full train application by means of a recess in the car body roof, leading to a mean contact force that is more independent from train speed and travelling direction.

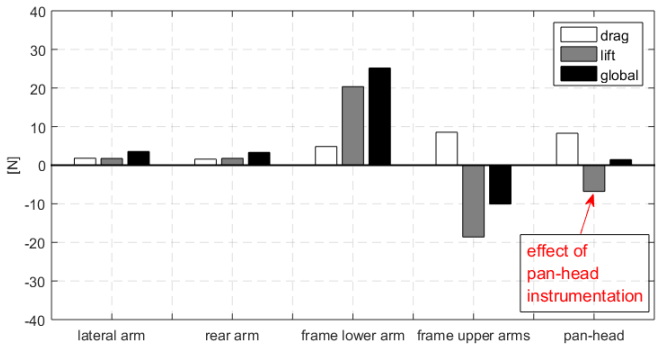

(a)

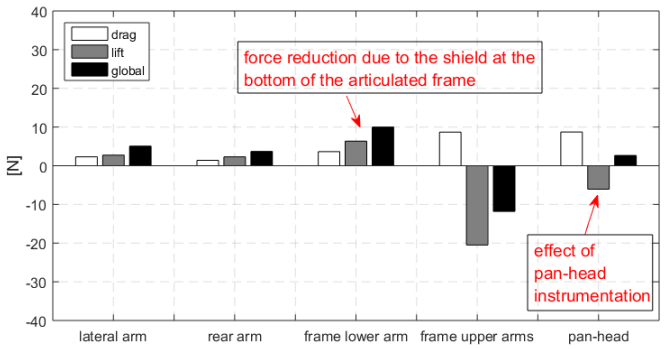

(b)

Figure 18: Comparison of the contribution of pantograph components to the total aerodynamic uplift for different test configurations (instrumented pantograph and pantograph with a shield at the bottom of the articulated frame). Knee-upstream orientation, height of 1.35 m, 40 m/s.

6. CONCLUSIONS

The paper investigated the influence of aerodynamic forces on a railway pantograph's aerodynamic uplift, which significantly affect the mean value of the contact force exerted by the pantograph on the overhead line. The analysis was carried out by means of both wind tunnel tests on a full-scale pantograph and CFD simulation in a wind tunnel scenario. The CFD model can be usefully adopted to evaluate numerical drag and lift forces acting on each single pantograph component, which is not easily performed experimentally, even in the wind tunnel. These forces can be used as the input of a procedure based on the virtual work principle, in order to evaluate the contribution of each different pantograph component to the total aerodynamic uplift. Due to the pantograph kinematics, the uplift is affected by both lift and drag forces acting on the single elements.

Steady RANS simulations appear sufficiently accurate to qualitatively reproduce the behaviour corresponding to different pantograph configurations, also giving satisfactory quantitative results, with computational effort compatible with their use at design stage. The most significant discrepancies were observed for pantograph components that are usually shielded, at least partially, in real line operation.

The proposed methodology can, therefore, be usefully adopted as an aid for the pantograph design and for the preliminary assessment of the pantograph's aerodynamic behaviour, keeping on-line tests only for final verification and eventual fine-tuning. The obtained results do not account for the

638 train roof boundary layer, which has the main effect of reducing the forces exerted on the lower
639 parts of the pantograph due to the reduced velocity of the incoming flow. The presence of the train
640 roof boundary layer should be considered (and simulated through the CFD calculation of the full
641 train) for the evaluation of the actual aerodynamic uplift in the final operating condition.

642
643 ## REFERENCES

[1] N. Zhou and W. Zhang, "Investigation on dynamic performance and parameter optimization design of pantograph and catenary system," *Finite Elements in Analysis and Design,* vol. 47, no. 3, pp. 288-295, 2011.

[2] S. Bruni, J. Ambrosio, . A. Carnicero, Y. H. Cho, L. Finner, M. Ikeda, S. Y. Kwon, J.-P. Massat, S. Stichel, M. Tur and W. Zhang, "The results of the pantograph-catenary interaction benchmark," *Vehicle System Dynamics,* vol. 53, no. 3, pp. 412-435, 2015.

[3] F. Resta, A. Facchinetti, A. Collina and G. Bucca, "On the use of a hardware in the loop set-up for pantograph dynamics evaluation," *Vehicle System Dynamics,* vol. 46, no. SUPPL.1 (In Memory of Joost Kalker), pp. 1039-1052, 2008.

[4] J. Pombo, J. Ambrosio, M. Pereira, F. Rauter , A. Collina and A. Facchinetti, "Influence of the aerodynamic forces on the pantograph-catenary system for high-speed trains," *Vehicle System Dynamics,* vol. 47, no. 11, pp. 1327-1347, 2009.

[5] Q. Lv, R. Li, S. Wang, N. Zhou and W. Zhang, "The Effect of the Working Height of Pantographs on Pantograph-Catenary Dynamic Performance," in *Proceedings of the second international conference on Railway Technology: Research, Development and Maintenance*, Ajaccio, Cordica (France), 2014.

[6] G. Bucca, M. Carnevale , A. Collina, A. Facchinetti, L. Drugge , P.-A. Jönsson and S. Stichel, "Adoption of different pantographs' preloads to improve multiple collection and speed up existing lines," *Vehicle System Dynamics,* vol. 50, no. supplement 1, pp. 403-418, 2012.

[7] M. Bocciolone, F. Resta , D. Rocchi, A. Tosi and A. Collina, "Pantograph aerodynamic effects on the pantograph–catenary interaction," *Vehicle System Dynamics,* vol. 44, no. sup1, pp. 560-570, 2006.

[8] Y. Lee, J. Rho, . M. Kwak , J. Lee, K. Kim and D. Lee, "Aerodynamic characteristics of high speed train pantograph with the optimized panhead shape," in *Proceedings of the seventh IASME/WSEAS international conference on fluid mechanics and aerodynamics*, Moscow, RussianFederation, 2009.

[9] M. Carnevale, A. Facchinetti and D. Rocchi, "Assessing aerodynamic effects on a railway pantograph by means of computational fluid dynamics," in *Proceedings of the third International conference on Railway Technology: Research, Development and Maintenance*, Cagliari (Italy), 2016.

[10] A. Collina, A. Lo Conte and M. Carnevale, "Effect of collector deformable modes in pantograph-catenary dynamic interaction," *Proceedings of the Institution of Mechanical Engineers, Part F: Journal*

of Rail and Rapid Transit, vol. 223, no. 1, pp. 1-14, 2009.

[11] J. L. a. W. Cho, "Prediction of low-speed aerodynamic load and aeroacoustic noise around simplified panhead section model," *Proc IMechE, Part F: J Rail Rapid Transit,* vol. 222, p. 423–431, 2008.

[12] M. Ikeda and T. Mitsumoji, "Numerical estimation of aerodynamic interference between panhead and articulated frame," *Q Rep of RTRI,* vol. 50, no. 4, p. 227–232, 2009.

[13] M. Suzuki, M. Ikeda and T. Koyama, "Flow control on pantograph with air intake and outlet," *Q Rep of RTRI,* vol. 48, no. 4, p. 236–239, 2007.

[14] M. Ikeda and T. Mitsumoji, "Evaluation Method of Low-Frequency Aeroacoustic Noise Source Structure Generated by Shinkansen Pantograph," *Quarterly Report of RTRI,* vol. 49, no. 3, pp. 184-190, 2008.

[15] S. Yao, D. Guo and G. Yang , "The influence of pantograph aerodynamic characteristics caused by its shroud," in *Proceedings of the first international workshop on high-speed and intercity railways*, Shenzhen, Hong Kong; China, 2011.

[16] J. Luo, J. Luo, Z. Yang, Y. Chen and . Z. Gao, "Numerical research on aerodynamic characteristic optimization of pantograph fixing place on high speed train," in *Proceedings of the 2nd Conference on Power Electronics and Intelligent Transportation System*, Shenzhen, China, 2009.

[17] R. Gregoire, A. Collina, F. Resta and D. Rocchi, "Some considerations on the aerodynamics of high speed pantograph: CFD and wind tunnel results," in *Proceedings of BBAA. The VI International Colloquium on: Bluff Bodies Aerodynamics & Applications*, Milano, Italy, 2008.

[18] R. Li, N. Zhou, G. Mei and W. Zhang, "Analysis of Pantograph-Catenary Dynamic Performance in Consideration of Fluid-Solid Coupled Vibration of Pantograph," in *Proceedings of the Second International Conference on Railway Technology: Research, Development and Maintenance*, Ajaccio, Corsica (France), 2014.

[19] T. Takaishi and . M. Ikeda, "Experimental method for wind tunnel tests to simulate turbulent flow on the roof of high-speed trains," *Q Rep of RTRI,* vol. 53, no. 3, p. 167–172, 2012.

[20] M. Carnevale, A. Facchinetti, L. Maggiori and D. Rocchi, "Computational fluid dynamics as a means of assessing the influence of aerodynamic forces on the mean contact force acting on a pantograph," *Proceedings of the Institution of Mechanical Engineers, Part F: Journal of Rail and Rapid Transit,* vol. 0, no. 0, first published on October 7, 2015.

[21] P. Catalano , M. Wang, G. Iaccarino and P. Moin, "Numerical simulation of the flow around a circular cylinder at high Reynolds numbers," *Int J Heat Fluid Flow,* no. 24, p. 463–469, 2003.

[22] . F. Menter, "Zonal two equation k-w turbulence models for aerodynamic flows," in *AIAA 93-2906, 24th Fluid Dynamics Conference,*, Orlando, Florida, 1993.

[23] S. Mandelli, S. Muggiasca and S. Malavasi, "Numerical simulation of an oscillating cylinder at high reynolds number," in *Proceedings of the International Conference on Offshore Mechanics and Arctic*

Engineering, OMAE, Nantes, France, 2013.

[24] S. Mandelli, S. Muggiasca and Malavasi, S., “Pressure field and wake modes analysis of an oscillating cylinder,” *Ocean Engineering,* vol. 124, pp. 74-83, 2016.

[25] Y. Lee, J. Rho, K. H. Kim, D. H. Lee and H. B. Kwon, “Experimental studies on the aerodynamic characteristics of a pantograph suitable for a high-speed train,” *Proceedings of the Institution of Mechanical Engineers, Part F: Journal of Rail and Rapid Transit,* vol. 229, no. 2, pp. 136-149, 2015.

644

645